J Eng Math (2013) 83:109–129
DOI 10.1007/s10665-012-9611-8

Generalized Weissinger's L-method for prediction of curved wings operating above a free surface in subsonic flow

H. Liang · Z. Zong · L. Sun · L. Zou · L. Zhou · Y. J. Zhao · Z. R. Ren

Received: 28 April 2011 / Accepted: 30 November 2012 / Published online: 27 April 2013

Abstract The classical Weissinger's L-method is generalized to the lifting problem for steadily advancing curved wings subject to the wing-in-ground (WIG) effect above a large body of water in subsonic flow, and the free surface defines the boundary between the air and water. Unlike the traditional analysis of the lifting problem, the essential techniques focus on finding the three-dimensional free surface Green's function generated by the isolated horseshoe vortex in the upper layer of the stratified fluid where the air is regarded as weakly compressible and the water is incompressible. The numerical calculation is implemented using Weissinger's L-method. Finally, the effects of the curved geometry on WIG effect in the vicinity of a free surface in subsonic flow are discussed. Extensive numerical examples are carried out to show the lift properties for three-dimensional swept and dihedral wings operating in the vicinity of a free surface as a function of the sweep or dihedral angle for different clearance-to-chord ratios and Mach numbers. Interestingly, for high Froude numbers, the free surface effectively becomes rigid, and it can safely be treated as a solid surface.

Keywords Curved wing · Free surface · Green's function · Stratified fluid · Weissinger's L-method · WIG effect

1 Introduction

Although the ship is one of the oldest forms of transportation, it is still subject to constant evolution. The high cost of fuel, coupled with increasing manufacturing and operating costs, has enabled the pursuit of high-performance

H. Liang · Z. Zong (✉) · L. Sun · L. Zhou · Y. J. Zhao · Z. R. Ren
School of Naval Architecture Engineering, State Key Laboratory of Structural Analysis for Industrial Equipment, Dalian University of Technology, Dalian 116024, People's Republic of China
e-mail: zongzhi@dlut.edu.cn

H. Liang
e-mail: lianghui128@126.com

L. Zou
School of Aeronautics and Astronautics, State Key Laboratory of Structural Analysis for Industrial Equipment, Dalian University of Technology, Dalian 116024, People's Republic of China

L. Zou
Department of Mathematics, Imperial College London, London SW7 2AZ, UK

unorthodox maritime vehicles. In recent years, there have been worldwide efforts to develop new conceptual vehicles focused on increasing the efficiency and economy of shipping operations [1]. The viscous and wave-making drags in water have become an obstacle to increasing ship speed without dramatically increasing the needed power, and then the excess power must be consumed. For the purpose of avoiding the aforementioned obstacle, wing-in-ground (WIG) effect crafts, which are lifted above the water surface by aerodynamic force, have become popular.

The study of the WIG effect was initiated in the early twentieth century in connection with the takeoff and landing of aircraft [2]. Research on the WIG effect has captured the attention of fluid dynamicists, applied mathematicians, computational scientists, and engineers [3, pp. 680]. This effect has already been studied by many other authors, but mainly with respect to vehicles moving near rigid walls. A well-known result is the increase in lift as the distance from the wing to the ground decreases. Even if it can be expected that this result will qualitatively hold also for liquid surfaces, a quantitative evaluation would be worthwhile together with an investigation of new phenomena possibly arising. Deformations of the free surface due to applied pressure loads may result in changes in aerodynamic performance.

Among the research on the lifting problem for WIG effect, experimental investigation still remains a powerful tool for predicting the aerodynamic parameters for a wing operating in proximity to a rigid wall. The flow field characteristics over the WIG effect were studied experimentally in a low-speed wind tunnel, and the aerodynamic parameters were obtained for different gap ratios [4]. The instantaneous and time-averaged flow properties of the wake region of the WIG effect with a finite trailing edge were identified. Furthermore, the generation, evolution, and breakdown of the wing edge vortex were studied experimentally [5]. The flow performances over the WIG effect were investigated in a low-speed wind tunnel with moving ground simulation for different attack angles and gap ratios. It was found that the geometry of the airfoil also had a strong influence on the aerodynamic characteristics [6].

Many numerical and theoretical studies on WIG effect in proximity to a solid surface have also been carried out. The unsteady aerodynamic forces acting on an oscillating wing in the vicinity of distant flat ground was studied using matched asymptotic expansions (MAEs) [7]. The method of MAEs was applied to the lifting problem for a wing in extreme ground effect. The general lifting surface problem was represented by a source-sink distribution on the upper surface of the wing and the wake. The results agree well with the numerical results from the lifting surface theory [8]. The boundary element method was used to investigate the aerodynamic characteristics of a wing flying over a rail and in a channel, and the method was determined to be valid based on comparisons with experimental results [9,10]. A numerical integration method was developed for the lifting surface and the Prandtl lifting line equation, and an image method was utilized to deal with the influence of the ground effect [11].

The development of computational fluid dynamics (CFD) spurred an interest in using this technique to deal with the lifting problem for WIG effect. Numerical analysis was performed to investigate the aerodynamic characteristics and static height stability of the endplate on the WIG effect. The Reynolds averaged Navier–Stokes equations were solved to predict the aerodynamic characteristics of the wing in ground effect [12]. Numerical simulations were performed to study the flow field about the oscillating airfoil in proximity to the ground. Inviscid and viscous turbulent flow simulations were carried out [13].

Although many theoretical and numerical studies have been conducted on the WIG effect in the presence of a rigid wall [4–13] showing that the lift force increases as the flight altitude decreases, very little attention has been paid to the ground effect lift performance above a free surface. Generally, the surface beneath a WIG effect craft, which is water, is assumed to be a rigid wall. Nevertheless, even purely static considerations show that the water surface should deform beneath the WIG effect craft, resulting in the variation of aerodynamic coefficients [14]. A wing moving above a free surface can generate water waves that propagate outward to infinity, complicating numerical and theoretical analysis. A very large water volume must be meshed if a numerical method is employed to solve the problem. It seems that only a few attempts have been made to investigate the WIG effect problem in the presence of a free surface, e.g., [15–18]. The panel method and Rankine source method were employed respectively to study the free surface effect on two-dimensional and three-dimensional WIG effects [15]. Three-dimensional free surface deformation due to the presence of the WIG effect was considered from a numerical position by CFD. The numerical results show that the tip vortices lead to free surface deformation [16]. In recent publications, the lift performance of the WIG effect in the presence of a free surface has been studied using Prandtl lifting line theory [17,18].

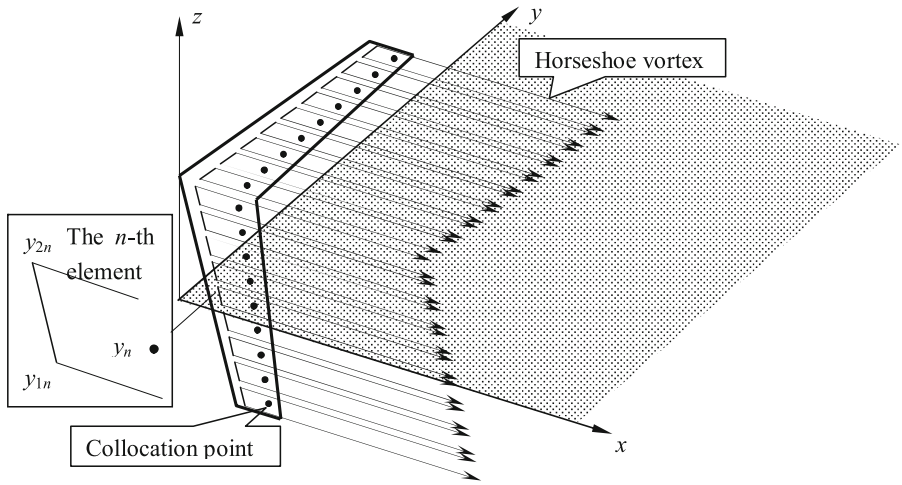

Fig. 1 Schematic figure of wing replaced by a sequence of horseshoe vortex elements in three-dimensional coordinate system

Usually, the velocity of the WIG effect craft ranges from 100 to 200 m/s and the Mach number is correspondingly from 0.3 to 0.6 in that case. When the Mach number is larger than 0.3, the compressibility of the air should be taken into consideration, and that flow regime can be defined as the subsonic flow. Thus, it is essential to analyze the compressibility effect on the lifting problem for WIG effect. For subsonic flow, density effects are important, but no shock wave appears.

The key techniques of Weissinger's L-method lie in dividing the thin wing planform into a finite number of elements and putting a horseshoe vortex on each of them, as shown in Fig. 1. The bound vortex is placed on the quarter-point line of the element, and the free vortices consist of two semifinite vortex filaments stretching backwards to infinity, the collocation point is at the three-quarter chord position measured from the leading edge. The strength of the vortex filament Γ is assumed to be constant for the horseshoe vortex. The kinematic flow condition—that zero normal flow passes across the wing's solid surface—should be satisfied at the collocation point [19].

The left and right wing halves around the longitudinal axis can deflect upward or downward, yielding a V-attitude of the wing configuration [20]. It is determined that the dihedral angle is positive as the wing halves deflect upward. A dihedral angle is applied by birds to keep good yaw stability. It can also affect the stability of an airfoil significantly and improve the stability of the airplane [21]. The doublet-lattice method was used to calculate the lift of the nonplanar wings including the one with a dihedral angle in proximity to a rigid wall based on the image method. It was found that the dihedral angle had a significant impact on the aerodynamic properties of the airplane [22].

A swept wing is a wing planform with a wing root to wingtip direction angled beyond (forward or afterward) the spanwise axis. The angle of sweep that characterizes a swept wing is conventionally measured along the one-quarter chord line [19]. A swept wing can efficiently decay the compressibility effect in the subsonic regime. Thus the research on the swept effect is of practical importance for a high-speed aircraft.

The present article is organized as follows. In Sect. 2, the governing equations in air and water are given, and the fully nonlinear kinematic and dynamic free surface boundary conditions are deduced. In Sect. 3, the nonlinear governing equation in air is linearized using a perturbation technique, and this approach is also utilized to linearize the nonlinear kinematic and dynamic free surface boundary conditions. Section 4 demonstrates the three-dimensional free surface Green's function for a horseshoe vortex in stratified fluid where the air is considered to be compressible and the water is incompressible. In Sects. 5 and 6, we analyze the cases of the dihedral wing and the swept wing operating close to the free surface. In Sect. 7, numerical results presented show the effects of the dihedral and swept geometry as well as the free surface effect on the aerodynamic properties of a wing in the vicinity of a free surface. In Sect. 8, a short conclusion is presented.

2 Governing equations and boundary conditions

In the present work, there are two layers of fluids, the air and the water. The air is treated as the weakly compressible; the water is incompressible. Throughout the article, the fluid is assumed to be inviscid, and the surface tension effect is neglected. Consider a horseshoe vortex element with a strength of Γ at a distance of h above the undisturbed free surface moving at a constant speed U. Thus, both air and water are disturbed. A three-dimensional Cartesian coordinate system $Oxyz$ is attached to the horseshoe vortex. The undisturbed free surface is on the Oxy plane and the Oz axis is positive upward (Fig. 2). Taking the horseshoe vortex as the frame of reference, the air and water move steadily at a velocity of U in the positive Ox direction.

2.1 Governing equations

Let U be the free stream speed in the positive x direction, as shown in Fig. 2. In the subsonic regime, U is always less than the speed of the sound propagating in air, U_{a0}. An important parameter in compressible flows is the Mach number, M_a, which is defined as $M_a = U/U_{a0}$.

Based on the assumption that the fluid is inviscid and barotropic, the governing equation for a compressible fluid in steady state can be written as [23, pp. 27]

$$\nabla^2\varphi_a - \frac{1}{U_{a0}^2}\mathbf{q}_a \cdot \nabla\frac{q_a^2}{2} = 0, \tag{1}$$

where φ_a denotes the perturbation velocity potential in air and $\mathbf{q}_a$ is the perturbation velocity component vector in air, which is defined as

$$\mathbf{q}_a = \nabla\varphi_a = u_a\mathbf{i} + v_a\mathbf{j} + w_a\mathbf{k}, \tag{2}$$

where u_a, v_a, and w_a denote the perturbation velocity components in air in the Ox, Oy, and Oz directions (Fig. 2).

However, the speed of a sound wave propagating in water is much greater than in air, and it can reach up to 1,400 m/s. This makes it possible to use a velocity potential whose gradient gives the fluid velocity components. The perturbation velocity potential must satisfy Laplace's equation everywhere in water,

$$\nabla^2\varphi_w = 0, \tag{3}$$

where the perturbation velocity potential in water is expressed using φ_w.

2.2 Boundary conditions

Taking the horseshoe vortex as the frame of reference, we can assume that the air and water can be seen as moving at a constant speed U (Fig. 2).

It is supposed that the free surface at infinity is undisturbed, and the pressure is the atmospheric pressure, p_0. Based on the irrotational and inviscid Bernoulli equation in incompressible and compressible flows, we obtain [24, Chap. 2]

$$\frac{p_a}{\rho_a} + g\zeta + \frac{1}{2}|U\mathbf{i} + \nabla\varphi_a|^2 = \frac{p_0}{\rho_a} + \frac{1}{2}U^2 \tag{4}$$

and

$$\frac{p_w}{\rho_w} + g\zeta + \frac{1}{2}|U\mathbf{i} + \nabla\varphi_w|^2 = \frac{p_w}{\rho_w} + \frac{1}{2}U^2, \tag{5}$$

where p_a and p_w denote the pressure on the interface in air and water and ζ denotes the free surface elevation. Due to the continuity in pressure on the interface, p_a should be equal to p_w. Then, by eliminating p_0, we obtain the fully nonlinear dynamic free surface condition

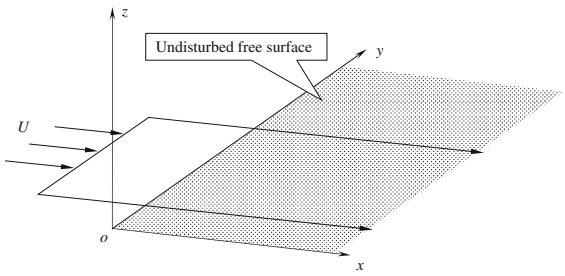

Fig. 2 Schematic illustration of flow past a horseshoe vortex over a free surface

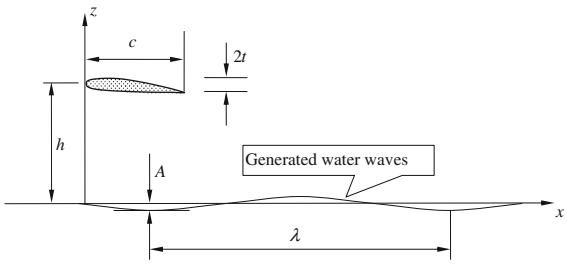

Fig. 3 Schematic figure of the foil operating over a free surface and its generated water waves

$$\rho_a\left[g\zeta + U\frac{\partial\varphi_a}{\partial x} + \frac{1}{2}\left(\frac{\partial\varphi_a}{\partial x}\right)^2 + \frac{1}{2}\left(\frac{\partial\varphi_a}{\partial y}\right)^2 + \frac{1}{2}\left(\frac{\partial\varphi_a}{\partial z}\right)^2\right]$$
$$= \rho_w\left[g\zeta + U\frac{\partial\varphi_w}{\partial x} + \frac{1}{2}\left(\frac{\partial\varphi_w}{\partial x}\right)^2 + \frac{1}{2}\left(\frac{\partial\varphi_w}{\partial y}\right)^2 + \frac{1}{2}\left(\frac{\partial\varphi_w}{\partial z}\right)^2\right] \quad \text{on} \quad z = \zeta\,(x, y)\,. \tag{6}$$

Suppose that the free surface equation is

$$F = z - \zeta\,(x, y) = 0. \tag{7}$$

By requiring that the substantial derivative of the quantity of $z - \zeta(x,\ y)$ vanishes on the mean free surface [25, pp. 239], we obtain the kinematic boundary condition for the free surface:

$$\frac{\partial\varphi_w}{\partial z} = \left(U + \frac{\partial\varphi_w}{\partial x}\right)\frac{\partial\zeta}{\partial x} + \frac{\partial\varphi_w}{\partial y}\frac{\partial\zeta}{\partial y} \quad \text{on} \quad z = \zeta\,(x, y) \tag{8}$$

and

$$\frac{\partial\varphi_a}{\partial z} = \left(U + \frac{\partial\varphi_a}{\partial x}\right)\frac{\partial\zeta}{\partial x} + \frac{\partial\varphi_a}{\partial y}\frac{\partial\zeta}{\partial y} \quad \text{on} \quad z = \zeta\,(x, y)\,. \tag{9}$$

In what follows, the characteristic nondimensional parameter is the clearance Froude number, which is defined as

$$\mathrm{Fr}_h = \frac{U}{\sqrt{gh}}, \tag{10}$$

where h is the clearance between the foil and the undisturbed free surface (Fig. 3).

3 Linearization procedure

3.1 Justification of linearization

In this study, it is assumed that the wing operating above the free surface is sufficiently thin. Thus we have

$$\frac{|\nabla\varphi_a|}{U} \ll 1. \tag{11}$$

Equation (11) indicates that the ratio of the perturbation velocity to the velocity of the incoming flow is sufficiently small, so the nonlinear governing equation in (1) can be linearized reasonably [23, Chap. 2].

For the water waves, if the velocity of the water wave propagation is given, the length of the water wave can be obtained [25, pp. 240]:

$$\lambda = \frac{2\pi U^2}{g}, \tag{12}$$

where λ represents the length of the generated water wave (Fig. 3). Thus, the length of the water wave is on the order of tens of kilometers. However, the magnitude order of the wave amplitude is on the order of meters, and then we have

$$\frac{A}{\lambda} \sim 10^{-3} \ll 1, \tag{13}$$

where A denotes the amplitude of the free surface wave, as shown in Fig. 3. From (13) it can be concluded that the generated water waves have a feature with macro amplitude; in addition, Scullen and Tuck [26] found that free surface deformation due to the passage of a pressure distribution, such as would be produced by a WIG effect craft or hovercraft, has the shape of a small-amplitude disturbance. Therefore, the linearized free surface condition is acceptable. We introduce a small parameter δ_1, which demonstrates the air–water interface free surface:

$$\delta_1 = \frac{A}{\lambda}. \tag{14}$$

On the basis of the thin wing assumption, the ratio

$$\delta_2 = \frac{t}{h} \tag{15}$$

should also be small, where t stands for half of the maximum thickness of the foil (Fig. 3).

We carry out the linearization procedure using the regular perturbation technique in which the sufficiently small parameters δ_1 and δ_2 are chosen. The free surface deformation induced by the foil has the same order as δ_1, which is verified in Appendix 1. Equations (14) and (15) allow the velocity potentials in air and water as well as the free surface deformation to be expanded in a power series in δ_1 and δ_2 as follows:

$$\varphi_a = \sum_{i=1}^{\infty} \delta_1^i \varphi_{a1}^{(i)} + \sum_{i=1}^{\infty} \delta_2^i \varphi_{a2}^{(i)}, \tag{16}$$

$$\varphi_w = \sum_{i=1}^{\infty} \delta_1^i \varphi_w^{(i)}, \tag{17}$$

and

$$\zeta = \sum_{i=1}^{\infty} \delta_1^i \zeta^{(i)}, \tag{18}$$

where $\varphi_{a1}^{(i)}, \varphi_w^{(i)}$, and $\zeta^{(i)}$, $i = 1, 2, \ldots$, denote the velocity potential in air and water and the free surface deformation in the form of the perturbation expansion function of the ith order with respect to δ_1, and $\varphi_{a2}^{(i)}$ denotes the velocity potential in air in the form of the perturbation expansion function of the ith order with respect to δ_2.

3.2 Linearization of governing equations

The governing equation in water is the Laplace equation as shown in Eq. (3) which shows linearity. Thus there is no need to conduct the linearization procedure. However, the governing equation in air is nonlinear, and thus the linearization procedure is necessary. We conduct the linearization procedure using a perturbation technique in which δ_1 and δ_2 are the small perturbation parameters, and they characterize some features of the interface between air and water and the thin foil.

Inserting Eq. (16) into Eq. (1), we can obtain a grouping like powers of δ_1 and δ_2, and a series of equations for each order of the solution can also be obtained. For the first-order term with respect to δ_1 and δ_2, the governing equation in the form of perturbation expansions can be expressed as

$$O(\delta_1): \ \nabla^2 \varphi_{a2}^{(1)} - M_a^2 \frac{\partial^2}{\partial x^2} \varphi_{a2}^{(1)} = 0 \tag{19a}$$

and

$$O(\delta_2):\ \nabla^2\varphi_{a2}^{(1)} - M_a^2\frac{\partial^2}{\partial x^2}\varphi_{a2}^{(1)} = 0. \tag{19b}$$

Then, the governing equation in air can be expressed as

$$\nabla^2\varphi_a^{(1)} - M_a^2\frac{\partial^2}{\partial x^2}\varphi_a^{(1)} = 0. \tag{20}$$

Equation (20) is the Prandtl–Glauert equation. We can introduce the scaling transformation

$$X = x/\beta,\ Y = y,\ Z = z, \tag{21}$$

where

$$\beta = \sqrt{1 - M_a^2}. \tag{22}$$

Then Eq. (21) can be written as

$$\frac{\partial^2\varphi_a^{(1)}}{\partial X^2} + \frac{\partial^2\varphi_a^{(1)}}{\partial Y^2} + \frac{\partial^2\varphi_a^{(1)}}{\partial Z^2} = 0. \tag{23}$$

The scaling transformation has stretched the x coordinate by $1/\beta$. After carrying out the scaling transformation, the elliptic partial differential equation (20) will be transformed into the Laplace equation. Suppose that the angle of attack of the wing is equal to α_0 in the original coordinate system, nevertheless it will be $1/\beta$ times the value of angle of attack in transformed coordinate system [24, Chap. 15]:

$$\alpha = \frac{1}{\beta}\alpha_0. \tag{24}$$

3.3 Linearization of free surface boundary condition equations

The approach that we use to linearize the kinematic and dynamic free surface boundary conditions is also the regular perturbation method in which the sufficiently small parameters δ_1 and δ_2 describing the interface between the water and air and the foil are selected as shown in Eqs. (14) and (15).

The perturbed velocity potentials in air and water can be expanded using Taylor series:

$$\varphi_a(x, y, \zeta) = \varphi_a(x, y, 0) + \zeta(x, y)\frac{\partial\varphi_a(x, y, 0)}{\partial z} + \frac{[\zeta(x, y)]^2}{2}\frac{\partial^2\varphi_a(x, y, 0)}{\partial z^2} + \cdots \tag{25}$$

and

$$\varphi_w(x, y, \zeta) = \varphi_w(x, y, 0) + \zeta(x, y)\frac{\partial\varphi_w(x, y, 0)}{\partial z} + \frac{[\zeta(x, y)]^2}{2}\frac{\partial^2\varphi_w(x, y, 0)}{\partial z^2} + \cdots. \tag{26}$$

By substituting Eqs. (17), (18), and (26) into the kinematic condition (8) in the water region, we can obtain a series of expansions with powers of δ_1. Since all the δ_1^n dependent terms must be equal. Thus, the perturbation expansion functions of the first-order with respect to δ_1 can be obtained:

$$O(\delta_1):\ \frac{\partial\varphi_w^{(1)}}{\partial z} = U\frac{\partial\zeta^{(1)}}{\partial x} \quad \text{at} \quad z = 0. \tag{27}$$

Similarly, substituting Eqs. (17), (18) and (25) into the kinematic condition (9) in the air region, we obtain the perturbation expansion functions of the first order with respect to δ_1 and δ_2:

$$O(\delta_1):\ \frac{\partial\varphi_{a1}^{(1)}}{\partial z} = U\frac{\partial\zeta^{(1)}}{\partial x} \quad \text{at} \quad z = 0 \tag{28}$$

and

$$O(\delta_2):\ \frac{\partial\varphi_{a2}^{(1)}}{\partial z} = 0 \quad \text{at} \quad z = 0. \tag{29}$$

Combining with Eqs. (27) and (28), we obtain

$$\frac{\partial \varphi_{a1}^{(1)}}{\partial z} = \frac{\partial \varphi_w^{(1)}}{\partial z} \quad \text{at} \quad z = 0. \tag{30}$$

We can conclude from Eqs. (29) and (30) that the velocity potential in air can be decomposed into two parts. One part satisfies the boundary condition of the rigid wall, which requires no flow crossing the boundary, as shown by Eq. (29), and the other one satisfies the condition prescribing the continuity in vertical velocity, as shown by Eq. (30).

Inserting Eqs. (16), (17), (18), (25), and (26) into the fully nonlinear dynamic free surface condition (6), we obtain the linearized dynamic free surface condition. Substituting Eqs. (27) and (28) into the linearized dynamic free surface condition and eliminating $\zeta^{(1)}$ yields

$$O(\delta_1): \ \rho_a \left[g \frac{\partial \varphi_{a1}^{(1)}}{\partial z} + U^2 \frac{\partial^2 \varphi_{a1}^{(1)}}{\partial x^2} \right] = \rho_w \left[g \frac{\partial \varphi_w^{(1)}}{\partial z} + U^2 \frac{\partial^2 \varphi_w^{(1)}}{\partial x^2} \right] \quad \text{at} \quad z = 0 \tag{31}$$

and

$$O(\delta_2): \ \frac{\partial^2 \varphi_{a2}^{(1)}}{\partial x^2} = 0 \quad \text{at} \quad z = 0. \tag{32}$$

Neglecting the superscripts in Eqs. (29)–(32) and consolidating φ_{a1} and φ_{a2} into φ_a, we can rewrite the free surface boundary conditions as

$$\frac{\partial \varphi_a}{\partial z} = \frac{\partial \varphi_w}{\partial z} \quad \text{at} \quad z = 0 \tag{33}$$

and

$$\rho_a \left(g \frac{\partial \varphi_a}{\partial z} + U^2 \frac{\partial^2 \varphi_a}{\partial x^2} \right) = \rho_w \left(g \frac{\partial \varphi_w}{\partial z} + U^2 \frac{\partial^2 \varphi_w}{\partial x^2} \right) \quad \text{at} \quad z = 0. \tag{34}$$

Equations (33) and (34) are in good agreement with the free surface boundary conditions for stratified fluid [27]. In Eqs. (33) and (34), φ_a can be composed of three parts: the velocity potential induced by the horseshoe vortex φ_{h0}, the image horseshoe vortex φ_{h1} beneath the free surface, and the velocity potential due to the free surface disturbance φ_f. Equation (29) indicates that the image horseshoe vortex has the same strength but the opposite sign. Thus, the sum of the vertical velocity induced by the horseshoe and its image at the mean free surface equals zero. Strictly speaking, the velocity potential of a three-dimensional vortex filament does not exist. The velocity potentials of the horseshoe vortex and its image can be replaced by the induced velocity components, and the induced velocities of these components can be computed using the Biot–Savart law. Based on the potential flow theory, the kinematic and dynamic boundary conditions (33) and (34) can be rewritten as

$$\frac{\partial \varphi_f}{\partial z} = \frac{\partial \varphi_w}{\partial z} \tag{35}$$

and

$$a \left(\frac{\partial u}{\partial x} + \frac{\partial u'}{\partial x} + k \frac{\partial \varphi_f}{\partial z} + \frac{\partial^2 \varphi_f}{\partial x^2} \right) = k \frac{\partial \varphi_w}{\partial z} + \frac{\partial^2 \varphi_w}{\partial x^2}, \tag{36}$$

where a is the density ratio of air to water and k, which denotes the wave number, equals g/U^2. In addition, u and u' denote the velocity components induced by the horseshoe vortex and the image in the Ox direction, respectively.

4 Green's function for a horseshoe vortex operating above a free surface

In Eqs. (35) and (36), the perturbation velocity induced by the horseshoe vortex in the Ox and Oz directions should be calculated. The horseshoe vortex is located in the air; thus the effect of compressibility should be taken into consideration. By applying the law of Biot–Savart [25], the induced velocity components can be obtained (the detailed derivation can be found in Appendix 2):

$$u = \frac{\Gamma}{4\pi^2} \int_0^{\infty} \int_{-\pi/2}^{\pi/2} \frac{\mathrm{i}}{\sin\theta} \exp\{m\,(z-h) + \mathrm{i}m\,[x\cos\theta/\beta + (y-y_{1n})\sin\theta]\}\,\mathrm{d}\theta\mathrm{d}m$$
$$- \frac{\Gamma}{4\pi^2} \int_0^{\infty} \int_{-\pi/2}^{\pi/2} \frac{\mathrm{i}}{\sin\theta} \exp\{m\,(z-h) + \mathrm{i}m\,[x\cos\theta/\beta + (y-y_{2n})\sin\theta]\}\,\mathrm{d}\theta\mathrm{d}m, \tag{37a}$$

$$u' = \frac{\Gamma}{4\pi^2} \int_0^{\infty} \int_{-\pi/2}^{\pi/2} \frac{\mathrm{i}}{\sin\theta} \exp\{-m\,(z+h) + \mathrm{i}m\,[x\cos\theta/\beta + (y-y_{1n})\sin\theta]\}\,\mathrm{d}\theta\mathrm{d}m$$
$$- \frac{\Gamma}{4\pi^2} \int_0^{\infty} \int_{-\pi/2}^{\pi/2} \frac{\mathrm{i}}{\sin\theta} \exp\{-m\,(z+h) + \mathrm{i}m\,[x\cos\theta/\beta + (y-y_{2n})\sin\theta]\}\,\mathrm{d}\theta\mathrm{d}m, \tag{37b}$$

and

$$w = \frac{\Gamma}{4\pi^2} \int_0^{\infty} \int_{-\pi/2}^{\pi/2} (\tan\theta + \cot\theta) \exp\{m\,(z-h) + \mathrm{i}m\,[x\cos\theta/\beta + (y-y_{1n})\sin\theta]\}\,\mathrm{d}\theta\mathrm{d}m$$
$$- \frac{\Gamma}{4\pi^2} \int_0^{\infty} \int_{-\pi/2}^{\pi/2} (\tan\theta + \cot\theta) \exp\{m\,(z-h) + \mathrm{i}m\,[x\cos\theta/\beta + (y-y_{2n})\sin\theta]\}\,\mathrm{d}\theta\mathrm{d}m, \tag{38a}$$

$$w' = -\frac{\Gamma}{4\pi^2} \int_0^{\infty} \int_{-\pi/2}^{\pi/2} (\tan\theta + \cot\theta) \exp\{-m\,(z+h) + \mathrm{i}m\,[x\cos\theta/\beta + (y-y_{1n})\sin\theta]\}\,\mathrm{d}\theta\mathrm{d}m$$
$$+ \frac{\Gamma}{4\pi^2} \int_0^{\infty} \int_{-\pi/2}^{\pi/2} (\tan\theta + \cot\theta) \exp\{-m\,(z+h) + \mathrm{i}m\,[x\cos\theta/\beta + (y-y_{2n})\sin\theta]\}\,\mathrm{d}\theta\mathrm{d}m, \tag{38b}$$

where y_{1n} and y_{2n} represent the coordinates of the two endpoints of bound line vortex as shown in Fig. 2, and they should satisfy $y_{1n} < y_{2n}$. In addition, the Fourier-type integration in the form of the inverse of the distance was used [28, Chap. 9]:

$$\frac{1}{r} = \frac{1}{\pi} \int_0^{\infty} \int_{-\pi/2}^{\pi/2} \exp\{m\,(z-h) + \mathrm{i}m\,[(x-\xi)\cos\theta + (y-\eta)\sin\theta]\}\,\mathrm{d}\theta\mathrm{d}m, \tag{39}$$

where

$$r = \sqrt{(x-\xi)^2 + (x-\xi)^2 + (z-h)^2}. \tag{40}$$

For the purpose of satisfying the governing equations, which are shown by Eqs. (19a, 19b), and (20), Eq. (39) can be rewritten in the form

$$\frac{1}{R} = \frac{1}{\pi} \int_0^{\infty} \int_{-\pi/2}^{\pi/2} \exp\{m\,(z-h) + \mathrm{i}m\,[(x-\xi)\cos\theta/\beta + (y-\eta)\sin\theta]\}\,\mathrm{d}\theta\mathrm{d}m, \tag{41}$$

where

$$R = \sqrt{(x-\xi)^2/\beta^2 + (x-\xi)^2 + (z-h)^2}. \tag{42}$$

The velocity potential in water should satisfy the Laplace equation (3). Thus, the expression of φ_w can be assumed to be in the form

$$\begin{aligned}\varphi_w &= \varphi_w(x, y, z)\\ &= \frac{\Gamma}{2\pi^2}\int_0^{\infty}\int_{-\pi/2}^{\pi/2} A(m,\theta)\exp\{m(z-h)+\mathrm{i}m[x\cos\theta+(y-y_{1n})\sin\theta]\}\,\mathrm{d}\theta\mathrm{d}m\\ &\quad -\frac{\Gamma}{2\pi^2}\int_0^{\infty}\int_{-\pi/2}^{\pi/2} A(m,\theta)\exp\{m(z-h)+\mathrm{i}m[x\cos\theta+(y-y_{2n})\sin\theta]\}\,\mathrm{d}\theta\mathrm{d}m. \end{aligned} \tag{43}$$

However, the velocity potential in air satisfies the governing equation (20). Thus, the expression of φ_f should satisfy the governing equation (20), and it can be expressed as

$$\begin{aligned}\varphi_f &= \varphi_f(x/\beta, y, z)\\ &= \frac{\Gamma}{2\pi^2}\int_0^{\infty}\int_{-\pi/2}^{\pi/2} B(m,\theta)\exp\{-m(z+h)+\mathrm{i}m[x\cos\theta/\beta+(y-y_{1n})\sin\theta]\}\,\mathrm{d}\theta\mathrm{d}m\\ &\quad -\frac{\Gamma}{2\pi^2}\int_0^{\infty}\int_{-\pi/2}^{\pi/2} B(m,\theta)\exp\{-m(z+h)+\mathrm{i}m[x\cos\theta/\beta+(y-y_{2n})\sin\theta]\}\,\mathrm{d}\theta\mathrm{d}m. \end{aligned} \tag{44}$$

Substituting Eqs. (37a,37b), (38a,38b), (43), and (44) into the kinematic and dynamic boundary conditions Eqs. (35) and (36), we obtain the expressions of the perturbation velocity potential in water and the velocity potential increment owing to the presence of a free surface:

$$\begin{aligned}\varphi_w &= -\frac{\Gamma}{2\pi^2}\int_0^{\infty}\int_{-\pi/2}^{\pi/2} \frac{a\beta\cos\theta\exp\{m(z-h)+\mathrm{i}m[x\cos\theta+(y-y_{1n})\sin\theta]\}}{\sin\theta\left(-a\beta^2k-am\cos^2\theta+\beta^2k-m\cos^2\theta\right)}\mathrm{d}\theta\mathrm{d}m\\ &\quad +\frac{\Gamma}{2\pi^2}\int_0^{\infty}\int_{-\pi/2}^{\pi/2} \frac{-a\beta\cos\theta\exp\{m(z-h)+\mathrm{i}m[x\cos\theta+(y-y_{2n})\sin\theta]\}}{\sin\theta\left(-a\beta^2k-am\cos^2\theta+\beta^2k-m\cos^2\theta\right)}\mathrm{d}\theta\mathrm{d}m. \end{aligned} \tag{45}$$

and

$$\begin{aligned}\varphi_f &= \frac{\Gamma}{2\pi^2}\int_0^{\infty}\int_{-\pi/2}^{\pi/2} \frac{a\beta\cos\theta\exp\{-m(z+h)+\mathrm{i}m[x\cos\theta/\beta+(y-y_{1n})\sin\theta]\}}{\sin\theta\left(-a\beta^2k-am\cos^2\theta+\beta^2k-m\cos^2\theta\right)}\mathrm{d}\theta\mathrm{d}m\\ &\quad -\frac{\Gamma}{2\pi^2}\int_0^{\infty}\int_{-\pi/2}^{\pi/2} \frac{a\beta\cos\theta\exp\{-m(z+h)+\mathrm{i}m[x\cos\theta/\beta+(y-y_{2n})\sin\theta]\}}{\sin\theta\left(-a\beta^2k-am\cos^2\theta+\beta^2k-m\cos^2\theta\right)}\mathrm{d}\theta\mathrm{d}m. \end{aligned} \tag{46}$$

Henceforth, in this article, the real part will be assumed to apply in all the complex expressions, and the symbol "Re" will be omitted. Evaluating the derivative of φ_f with respect to z, we obtain the velocity of downwash induced by the free surface disturbance:

$$\begin{aligned}\frac{\partial \varphi_f}{\partial z} = &-\frac{\Gamma}{4\pi^2}\int_0^{\infty}\int_{-\pi/2}^{\pi/2}\frac{a\beta\exp\{-m(z+h)+\mathrm{i}m[x\cos\theta/\beta+(y-y_{1n})\sin\theta]\}}{(1+a)\sin\theta\cos\theta}\mathrm{d}\theta\mathrm{d}m\\ &+\frac{\Gamma}{4\pi^2}\int_0^{\infty}\int_{-\pi/2}^{\pi/2}\frac{a\beta\exp\{-m(z+h)+\mathrm{i}m[x\cos\theta/\beta+(y-y_{2n})\sin\theta]\}}{(1+a)\sin\theta\cos\theta}\mathrm{d}\theta\mathrm{d}m\\ &-\frac{\Gamma}{2\pi^2}\int_0^{\infty}\int_{-\pi/2}^{\pi/2}\frac{a(1-a)\beta^3k}{(1+a)^2\sin\theta\cos^3\theta}\cdot\frac{\exp\{-m(z+h)+\mathrm{i}m[x\cos\theta/\beta+(y-y_{1n})\sin\theta]\}}{m-\frac{1-a}{1+a}\beta^2k\sec^2\theta}\mathrm{d}\theta\mathrm{d}m\\ &+\frac{\Gamma}{2\pi^2}\int_0^{\infty}\int_{-\pi/2}^{\pi/2}\frac{a(1-a)\beta^3k}{(1+a)^2\sin\theta\cos^3\theta}\cdot\frac{\exp\{-m(z+h)+\mathrm{i}m[x\cos\theta/\beta+(y-y_{2n})\sin\theta]\}}{m-\frac{1-a}{1+a}\beta^2k\sec^2\theta}\mathrm{d}\theta\mathrm{d}m.\end{aligned} \tag{47}$$

In Eq. (47), the image term can be integrated directly using a numerical integration method, such as the Gaussian quadrature method. However, the last two terms contain improper integrals with singularities as

$$m-\frac{1-a}{1+a}\beta^2k\sec^2\theta=0, \tag{48}$$

and evaluating this kind of double integral directly is a rather time-consuming numerical task. For the purpose of obtaining the value of the integration quickly but precisely, we can rewrite the last two terms in the forms $\mathrm{e}^{\lambda}E_1(\lambda)$, which can be found in [29]

$$\begin{aligned}\frac{\partial \varphi_f}{\partial z} = &-\frac{\Gamma}{4\pi^2}\int_0^{\infty}\int_{-\pi/2}^{\pi/2}\frac{a\beta\exp\{-m(z+h)+\mathrm{i}m[x\cos\theta/\beta+(y-y_{1n})\sin\theta]\}}{(1+a)\sin\theta\cos\theta}\mathrm{d}\theta\mathrm{d}m\\ &+\frac{\Gamma}{4\pi^2}\int_0^{\infty}\int_{-\pi/2}^{\pi/2}\frac{a\beta\exp\{-m(z+h)+\mathrm{i}m[x\cos\theta/\beta+(y-y_{2n})\sin\theta]\}}{(1+a)\sin\theta\cos\theta}\mathrm{d}\theta\mathrm{d}m\\ &-\frac{\Gamma}{2\pi^2}\int_{-\pi/2}^{\pi/2}\frac{a(1-a)\beta^3k}{(1+a)^2\sin\theta\cos^3\theta}\left[\mathrm{e}^{\lambda_1}E_1(\lambda_1)-\mathrm{e}^{\lambda_2}E_1(\lambda_2)+2\pi\mathrm{i}H(x)\left(\mathrm{e}^{\lambda_1}-\mathrm{e}^{\lambda_2}\right)\right]\mathrm{d}\theta,\end{aligned} \tag{49}$$

where the Heaviside function $H(x)$ is equal to 1 when x is positive and equal to 0 when x is less than or equal to 0. In addition, λ_i is

$$\lambda_i=\beta^2k\sec^2\theta\frac{1-a}{1+a}\{-(z+h)+\mathrm{i}[x\cos\theta/\beta+(y-y_{in})\sin\theta]\},\quad i=1,2. \tag{50}$$

The exponential integral function $E_1(x)$ is

$$E_1(x)=\int_x^{\infty}\frac{\mathrm{e}^{-t}}{t}\mathrm{d}t. \tag{51}$$

The expression $\mathrm{e}^{\lambda}E_1(\lambda)$ in Eq. (49) can be evaluated using the Padé approximation [30], which can accurately and efficiently convert the improper integral to a polynomial, reducing the complexity and computing time [26].

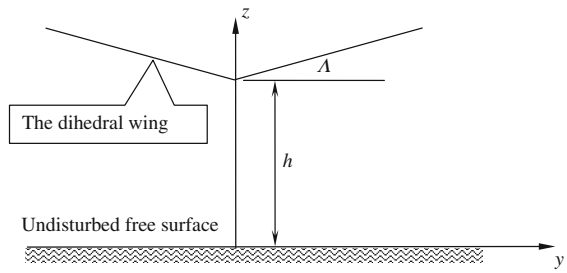

Fig. 4 Dihedral wing over free surface at clearance of h measured from central plan

5 Dihedral effect on WIG effect in vicinity of free surface

The dihedral angle can determine the dihedral effect, and the dihedral effect is a critical factor in the stability of an aircraft about the roll axis [21]. It is also pertinent to the nature of an aircraft's roll oscillation and to maneuverability about the roll axis.

The WIG effect with a dihedral angle close to a solid surface is discussed in [22]. Thus there is no longer any need to represent it. We simply study the WIG effect with dihedral in proximity to a free surface. We assume a steady motion of a thin three-dimensional wing with dihedral at the clearance of h over the air–water interface free surface, as shown in Fig. 4.

For a wing with dihedral, the function of the one-quarter chord $f(y)$ with respect to y in the original coordinate system can be expressed as

$$f(y) = \tan \Lambda \cdot |y| + h, \tag{52}$$

where Λ is a dihedral angle (Fig. 4). However, in the transformed coordinate system, the one-quarter chord function becomes

$$f(Y) = \tan \Lambda \cdot |Y| + h. \tag{53}$$

Due to the deflection of the one-quarter chord line, the perturbation velocity components induced by the horseshoe vortex on the nth element of the dihedral wing in the Ox and Oz directions can be obtained:

$$\begin{aligned} u_n =& \frac{\Gamma_n}{4\pi^2} \int_0^{\infty} \int_{-\pi/2}^{\pi/2} \frac{\mathrm{i}}{\sin\theta} \exp\{m\,[z - f\,(y_{1n})] + \mathrm{i}m\,[x\cos\theta/\beta + (y - y_{1n})\sin\theta]\}\,\mathrm{d}\theta\mathrm{d}m \\ & - \frac{\Gamma_n}{4\pi^2} \int_0^{\infty} \int_{-\pi/2}^{\pi/2} \frac{\mathrm{i}}{\sin\theta} \exp\{m\,[z - f\,(y_{2n})] + \mathrm{i}m\,[x\cos\theta/\beta + (y - y_{2n})\sin\theta]\}\,\mathrm{d}\theta\mathrm{d}m, \end{aligned} \tag{54a}$$

$$\begin{aligned} u_n' =& \frac{\Gamma_n}{4\pi^2} \int_0^{\infty} \int_{-\pi/2}^{\pi/2} \frac{\mathrm{i}}{\sin\theta} \exp\{-[z + f\,(y_{1n})] + \mathrm{i}m\,[x\cos\theta/\beta + (y - y_{1n})\sin\theta]\}\,\mathrm{d}\theta\mathrm{d}m \\ & - \frac{\Gamma_n}{4\pi^2} \int_0^{\infty} \int_{-\pi/2}^{\pi/2} \frac{\mathrm{i}}{\sin\theta} \exp\{-[z + f\,(y_{2n})] + \mathrm{i}m\,[x\cos\theta/\beta + (y - y_{2n})\sin\theta]\}\,\mathrm{d}\theta\mathrm{d}m, \end{aligned} \tag{54b}$$

and

$$w_n = \frac{\Gamma_n}{4\pi^2}\int_0^{\infty}\int_{-\pi/2}^{\pi/2}(\tan\theta+\cot\theta)\exp\{m[z-f(y_{1n})]+\mathrm{i}m[x\cos\theta/\beta+(y-y_{1n})\sin\theta]\}\,\mathrm{d}\theta\mathrm{d}m - \frac{\Gamma_n}{4\pi^2}\int_0^{\infty}\int_{-\pi/2}^{\pi/2}(\tan\theta+\cot\theta)\exp\{m[z-f(y_{2n})]+\mathrm{i}m[x\cos\theta/\beta+(y-y_{2n})\sin\theta]\}\,\mathrm{d}\theta\mathrm{d}m, \tag{55a}$$

$$w_n' = -\frac{\Gamma_n}{4\pi^2}\int_0^{\infty}\int_{-\pi/2}^{\pi/2}(\tan\theta+\cot\theta)\exp\{-[z+f(y_{1n})]+\mathrm{i}m[x\cos\theta/\beta+(y-y_{1n})\sin\theta]\}\,\mathrm{d}\theta\mathrm{d}m + \frac{\Gamma_n}{4\pi^2}\int_0^{\infty}\int_{-\pi/2}^{\pi/2}(\tan\theta+\cot\theta)\exp\{-[z+f(y_{2n})]+\mathrm{i}m[x\cos\theta/\beta+(y-y_{2n})\sin\theta]\}\,\mathrm{d}\theta\mathrm{d}m, \tag{55b}$$

where Γ_n is the circulation of the horseshoe vortex on the nth element. Evaluating the derivative of Eq. (49) with respect to z at the collocation point, we obtain the velocity of the downwash on the collocation point of the mth element, which is induced by the free surface disturbance terms with respect to the horseshoe vortex on the nth element:

$$\begin{aligned} w_{sf}^{m,n} &= \left.\frac{\partial\varphi_f}{\partial z}\right|_{z=f(y_m),y=y_m,x=\beta c/2} \\ &= -\frac{\Gamma}{2\pi^2}\int_0^{\infty}\int_{-\pi/2}^{\pi/2}\frac{a\beta\exp\{-m[f(y_m)-f(y_{1n})]+\mathrm{i}m[c\cos\theta/2+(y-y_{1n})\sin\theta]\}}{(1+a)\sin\theta\cos\theta}\mathrm{d}\theta\mathrm{d}m \\ &\quad+\frac{\Gamma}{2\pi^2}\int_0^{\infty}\int_{-\pi/2}^{\pi/2}\frac{a\beta\exp\{-m[f(y_m)-f(y_{2n})]+\mathrm{i}m[c\cos\theta/2+(y-y_{2n})\sin\theta]\}}{(1+a)\sin\theta\cos\theta}\mathrm{d}\theta\mathrm{d}m \\ &\quad-\frac{\Gamma}{2\pi^2}\int_{-\pi/2}^{\pi/2}\frac{a(1-a)\beta^3k}{(1+a)^2\sin\theta\cos^3\theta}\left[\mathrm{e}^{\lambda_1}E_1(\lambda_1)-\mathrm{e}^{\lambda_2}E_1(\lambda_2)+2\pi\mathrm{i}\left(\mathrm{e}^{\lambda_1}-\mathrm{e}^{\lambda_2}\right)\right]\mathrm{d}\theta, \end{aligned} \tag{56}$$

where $w_{sf}^{m,n}$ denotes the velocity of downwash on the collocation point on the mth element, which is induced by the free surface disturbance terms with respect to the horseshoe vortex on the nth element, and y_m is the coordinate of the collocation point on the mth element, as shown in Fig. 1, and

$$\lambda_i = \beta^2k\sec^2\theta\frac{1-a}{1+a}\{-[f(y_m)-f(y_{in})]+\mathrm{i}[c\cos\theta/2+(y-y_{in})\sin\theta]\},\quad i=1,2. \tag{57}$$

Due to the presence of the free surface, the induced velocity in the direction of the movement exists. We can calculate it by taking the derivative of Eq. (49) with respect to x:

$$\begin{aligned} u_f^{m,n} &= \left.\frac{\partial\varphi_f}{\partial x}\right|_{z=f(y_m),y=y_m,x=0} \\ &= \frac{\Gamma_n}{4\pi^2}\int_0^{\infty}\int_{-\pi/2}^{\pi/2}\frac{2\mathrm{i}a}{(1+a)\sin\theta}\exp\{-m[z+f(y_{1n})]+\mathrm{i}m(y-y_{1n})\sin\theta\}\,\mathrm{d}\theta\mathrm{d}m \\ &\quad-\frac{\Gamma_n}{4\pi^2}\int_0^{\infty}\int_{-\pi/2}^{\pi/2}\frac{2\mathrm{i}a}{(1+a)\sin\theta}\exp\{-m[z+f(y_{1n})]+\mathrm{i}m(y-y_{1n})\sin\theta\}\,\mathrm{d}\theta\mathrm{d}m \end{aligned}$$

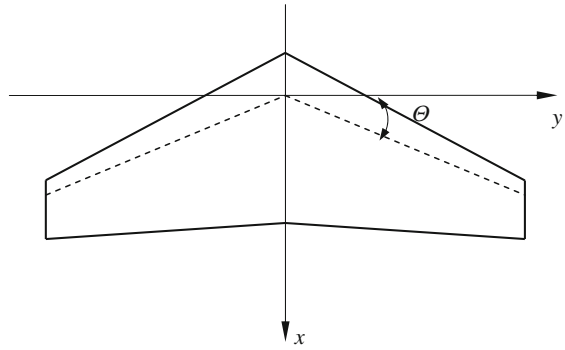

Fig. 5 Schematic of swept wing in two-dimensional coordinate system

$$+\frac{\Gamma}{2\pi^2}\int_{-\pi/2}^{\pi/2}\frac{\mathrm{i}a\,(1-a)\,\beta^2 k}{(1+a)^2\sin\theta\cos^2\theta}\left[\mathrm{e}^{\lambda_1}E_1\,(\lambda_1)-\mathrm{e}^{\lambda_2}E_1\,(\lambda_2)+2\pi\mathrm{i}\left(\mathrm{e}^{\lambda_1}-\mathrm{e}^{\lambda_2}\right)\right]\mathrm{d}\theta, \tag{58}$$

where $u_f^{m,n}$ denotes the perturbation velocity on the mth element in the direction of the incoming flow generated by the disturbance of the free surface induced by the horseshoe vortex on the nth element, and

$$\lambda_i=\beta^2 k\sec^2\theta\frac{1-a}{1+a}\left\{-\left[f\,(y_m)-f\,(y_{in})\right]+\mathrm{i}\,(y-y_{in})\sin\theta\right\},\quad i=1,2. \tag{59}$$

6 Swept effect on WIG effect in proximity to a free surface

In the subsonic regime, the swept effect is of practical importance. It can delay the onset of the compressibility effect. We assume a steady motion of a thin flat three-dimensional swept wing at a clearance of h over an undisturbed free surface and the angle of sweep is Λ (Fig. 5).

For the wing with sweep, the function of one-quarter chord $g(y)$ with respect to y in the original coordinate system is

$$g(y)=\tan\Theta\cdot|y|, \tag{60}$$

where Θ is the sweep angle, taken to be positive for afterward deflection (Fig. 5). However, the function of $g(y)$ will be changed because of the stretching of the x coordinate caused by the scaling transformation. The slope of $G(y)$ in the transformed coordinate system is $1/\beta$ times the value of the slope in the original coordinate system:

$$G(Y)=\frac{\tan\Theta}{\beta}\cdot|Y|. \tag{61}$$

Due to the curvature of the one-quarter chord line, the perturbation velocity components induced by the horseshoe vortex on the swept wing in the Ox and Oz directions can be expressed as

$$\begin{aligned}u_n=&\frac{\Gamma_n}{4\pi^2}\int_0^{\infty}\int_{-\pi/2}^{\pi/2}\frac{\mathrm{i}}{\sin\theta}\exp\left(m\,(z-h)+\mathrm{i}m\left\{\left[x/\beta-G\,(y_{1n})\right]\cos\theta+(y-y_{1n})\sin\theta\right\}\right)\mathrm{d}\theta\mathrm{d}m\\&-\frac{\Gamma_n}{4\pi^2}\int_0^{\infty}\int_{-\pi/2}^{\pi/2}\frac{\mathrm{i}}{\sin\theta}\exp\left(m\,(z-h)+\mathrm{i}m\left\{\left[x/\beta-G\,(y_{2n})\right]\cos\theta+(y-y_{2n})\sin\theta\right\}\right)\mathrm{d}\theta\mathrm{d}m,\end{aligned} \tag{62a}$$

$$u_n'=\frac{\Gamma_n}{4\pi^2}\int_0^{\infty}\int_{-\pi/2}^{\pi/2}\frac{\mathrm{i}}{\sin\theta}\exp\left(-m\,(z+h)+\mathrm{i}m\left\{\left[x/\beta-G\,(y_{1n})\right]\cos\theta+(y-y_{1n})\sin\theta\right\}\right)\mathrm{d}\theta\mathrm{d}m$$

$$-\frac{\Gamma_n}{4\pi^2}\int_0^{\infty}\int_{-\pi/2}^{\pi/2}\frac{\mathrm{i}}{\sin\theta}\exp\left(-m\left(z+h\right)+\mathrm{i}m\left\{\left[x/\beta-G\left(y_{2n}\right)\right]\cos\theta+\left(y-y_{2n}\right)\sin\theta\right\}\right)\mathrm{d}\theta\mathrm{d}m, \tag{62b}$$

and

$$\begin{aligned}w_n=&\frac{\Gamma_n}{4\pi^2}\int_0^{\infty}\int_{-\pi/2}^{\pi/2}\left(\tan\theta+\cot\theta\right)\exp\left(m\left(z-h\right)+\mathrm{i}m\left\{\left[x/\beta-G\left(y_{1n}\right)\right]\cos\theta+\left(y-y_{1n}\right)\sin\theta\right\}\right)\mathrm{d}\theta\mathrm{d}m\\&-\frac{\Gamma_n}{4\pi^2}\int_0^{\infty}\int_{-\pi/2}^{\pi/2}\left(\tan\theta+\cot\theta\right)\exp\left(m\left(z-h\right)+\mathrm{i}m\left\{\left[x/\beta-G\left(y_{2n}\right)\right]\cos\theta+\left(y-y_{2n}\right)\sin\theta\right\}\right)\mathrm{d}\theta\mathrm{d}m,\end{aligned} \tag{63a}$$

$$\begin{aligned}w_n'=&\frac{-\Gamma_n}{4\pi^2}\int_0^{\infty}\int_{-\pi/2}^{\pi/2}\left(\tan\theta+\cot\theta\right)\exp\left(-m\left(z+h\right)+\mathrm{i}m\left\{\left[x/\beta-G\left(y_{1n}\right)\right]\cos\theta+\left(y-y_{1n}\right)\sin\theta\right\}\right)\mathrm{d}\theta\mathrm{d}m\\&+\frac{\Gamma_n}{4\pi^2}\int_0^{\infty}\int_{-\pi/2}^{\pi/2}\left(\tan\theta+\cot\theta\right)\exp\left(-m\left(z+h\right)+\mathrm{i}m\left\{\left[x/\beta-G\left(y_{2n}\right)\right]\cos\theta+\left(y-y_{2n}\right)\sin\theta\right\}\right)\mathrm{d}\theta\mathrm{d}m.\end{aligned} \tag{63b}$$

Evaluating the derivative of (49) with respect to z, we obtain the velocity of downwash on the collocation point of the mth element, which is induced by the velocity potential increment caused by the horseshoe vortex on the nth element:

$$\begin{aligned}w_{sf}^{m,n}=&\left.\frac{\partial\varphi_f}{\partial z}\right|_{z=h,y=y_m,x=\beta c/2+G(y_m)}\\=&-\frac{\Gamma_n}{2\pi^2}\int_0^{\infty}\int_{-\pi/2}^{\pi/2}\frac{a\beta\exp(-2mh+\mathrm{i}m\left\{\left[c/2+G\left(y_m\right)-G\left(y_{1n}\right)\right]\cos\theta+\left(y-y_{1n}\right)\sin\theta\right\})}{\left(1+a\right)\sin\theta\cos\theta}\mathrm{d}\theta\mathrm{d}m\\&+\frac{\Gamma_n}{2\pi^2}\int_0^{\infty}\int_{-\pi/2}^{\pi/2}\frac{a\beta\exp(-2mh+\mathrm{i}m\left\{\left[c/2+G\left(y_m\right)-G\left(y_{2n}\right)\right]\cos\theta+\left(y-y_{2n}\right)\sin\theta\right\})}{\left(1+a\right)\sin\theta\cos\theta}\mathrm{d}\theta\mathrm{d}m\\&-\frac{\Gamma_n}{2\pi^2}\int_{-\pi/2}^{\pi/2}\frac{a\left(1-a\right)\beta^3\left\{\mathrm{e}^{\lambda_1}E_1\left(\lambda_1\right)-\mathrm{e}^{\lambda_2}E_1\left(\lambda_2\right)+2\pi\mathrm{i}H\left[c/2+G\left(y_m\right)-G\left(y_{in}\right)\right]\left(\mathrm{e}^{\lambda_1}-\mathrm{e}^{\lambda_2}\right)\right\}k}{\left(1+a\right)^2\sin\theta\cos^3\theta}\mathrm{d}\theta,\end{aligned} \tag{64}$$

where

$$\lambda_i=\beta^2k\sec^2\theta\frac{1-a}{1+a}(-2h+\mathrm{i}\left\{\left[c/2+G\left(y_m\right)-G\left(y_{in}\right)\right]\cos\theta+\left(y-y_{in}\right)\sin\theta\right\}),\quad i=1,2. \tag{65}$$

Similarly, the induced velocity in the direction of the movement exists. We can calculate it by taking the derivative of Eq. (49) with respect to x:

$$\begin{aligned}u_f^{m,n}=&\left.\frac{\partial\varphi_f}{\partial x}\right|_{z=h,y=y_m,x=G(y_m)}\\=&\frac{\Gamma_n}{2\pi^2}\int_0^{\infty}\int_{-\pi/2}^{\pi/2}\frac{\mathrm{i}a\exp\left(-2mh+\mathrm{i}m\left\{\left[G\left(y_m\right)-G\left(y_{1n}\right)\right]\cos\theta+\left(y-y_{1n}\right)\sin\theta\right\}\right)}{\left(1+a\right)\sin\theta}\mathrm{d}\theta\mathrm{d}m\end{aligned}$$

$$-\frac{\Gamma_n}{2\pi^2}\int_0^{\infty}\int_{-\pi/2}^{\pi/2}\frac{\mathrm{i}a\exp\left(-2mh+\mathrm{i}m\left\{\left[G\left(y_m\right)-G\left(y_{2n}\right)\right]\cos\theta+\left(y-y_{2n}\right)\sin\theta\right\}\right)}{(1+a)\sin\theta}\mathrm{d}\theta\mathrm{d}m$$

$$+\frac{\Gamma_n}{2\pi^2}\int_{-\pi/2}^{\pi/2}\frac{\mathrm{i}a\left(1-a\right)\beta^2k}{(1+a)^2\sin\theta\cos^2\theta}\left\{\mathrm{e}^{\lambda_1}E_1\left(\lambda_1\right)-\mathrm{e}^{\lambda_2}E_1\left(\lambda_2\right)+2\pi\mathrm{i}H\left[G\left(y_m\right)-G\left(y_{in}\right)\right]\left(\mathrm{e}^{\lambda_1}-\mathrm{e}^{\lambda_2}\right)\right\}\mathrm{d}\theta, \tag{66}$$

where

$$\lambda_i=\beta^2k\sec^2\theta\frac{1-a}{1+a}(-2h+\mathrm{i}\left\{\left[G\left(y_m\right)-G\left(y_{in}\right)\right]\cos\theta+\left(y-y_{in}\right)\sin\theta\right\}),\quad i=1,2. \tag{67}$$

7 Results and discussion

Generally, a wing is symmetrical about the central plane. Suppose that the wing's semispan can be divided into N elements; therefore, there are $2N$ elements on the wing surface. The induced velocity of downwash at the collocation point of the mth element is the sum of the velocity of downwash induced by the horseshoe vortices on all the elements from 1 to $2N$ on the wing surface as well as their image terms and the free surface disturbance terms

$$w_s^w=\sum\nolimits_{n=1}^{2N}\left[w_s^{m,n}+w_s'^{m,n}+\mathrm{Re}\left(w_{sf}^{m,n}\right)\right], \tag{68}$$

where $w_s^{m,n}$ and $w_s'^{m,n}$ denote the velocity of downwash at the collocation point of the mth element induced by the horseshoe vortex and its image on the nth element, which can be calculated using the law of Biot–Savart. Suppose that the movement velocity of the wing is U, and we can calculate the velocity of the incoming flow for the mth element:

$$u^m=U+u'^{m,n}+\sum\nolimits_{n=1}^{2N}\mathrm{Re}\left(u_f^{m,n}\right). \tag{69}$$

In addition, the boundary condition prescribing zero normal flow across the wing's solid surface should be satisfied:

$$w_s^m=u^m\alpha^m, \tag{70}$$

where α^m represents the angle of attack for the mth element. Then a system of linear algebraic equations needs to be solved to determine the strength of the horseshoe vortex on each element. Then the lift coefficient can be calculated:

$$C_{\mathrm{L}}=\frac{2}{\rho U^2S}\sum_{n=1}^{2N}\rho u^m\Gamma_m\left|y_{2m}-y_{1m}\right|, \tag{71}$$

where S denotes the area of the wing surface.

In accordance with Eq. (71), the lifting force acting on the wing in the vicinity of a free surface can be obtained. The ratio of C_{L} to C_{LR} for a flat wing with an aspect ratio of 4.0 is computed to study the influence of the clearance Froude number on the lift performance, as shown in Fig. 6a–d, where C_{L} denotes the lift coefficient for a wing operating above a free surface, and C_{LR} is the lift coefficient for the case of a rigid wall, which can be calculated by the method of images [19].

It can be observed from Fig. 6 that the amplitude of the ratio of C_{L} to C_{LR} can reach up to 8 % as the clearance-to-chord ratio h/c equals 0.1, and the free surface effect must be taken into consideration in this case. As the clearance-to-chord ratio h/c equals 0.2, the amplitude is much smaller, which is equal to 1.5 %; the amplitude decreases to less than 0.2 % at $h/c=0.5$. As shown by Fig. 6a–d, the amplitude decays fairly quickly with decreasing clearance. The amplitude decays to less than 0.05 % as the clearance-to-chord h/c equals 1.0. As a

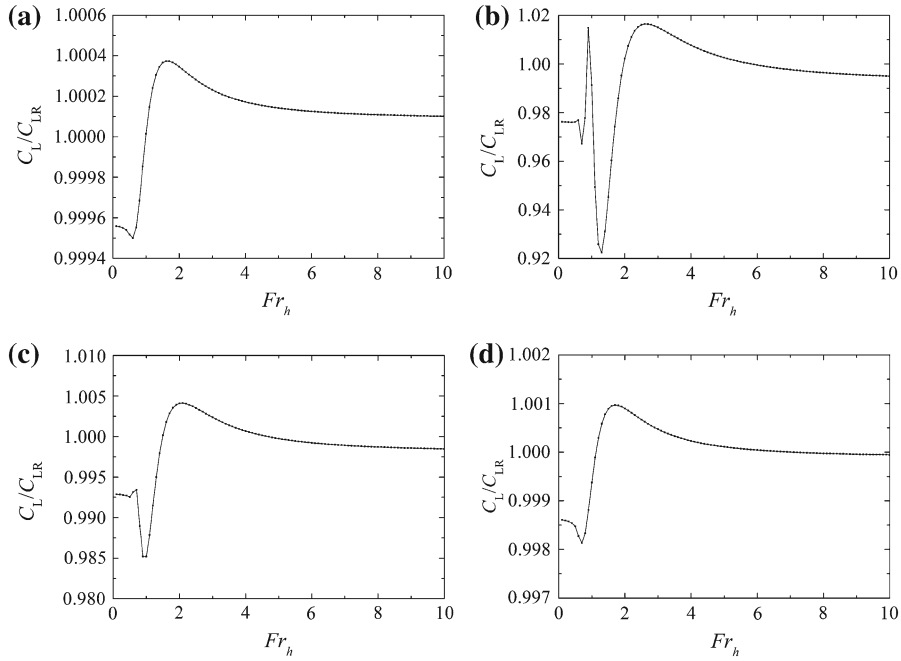

Fig. 6 Ratio of C_L to C_{LR} versus clearance Froude number for different clearance-to-chord ratios. **a** $h/c = 0.1$. **b** $h/c = 0.2$. **c** $h/c = 0.5$. **d** $h/c = 1.0$

consequence, the free surface disturbance effect can be neglected and the free surface can be regarded as a rigid wall for the case of a clearance-to-chord ratio of greater than 0.2 if the error limit is no more than 2 %.

Moreover, the ratio of C_L to C_{LR} fluctuates sharply as the clearance Froude number is close to 1.0. The factors leading to this phenomenon are mainly twofold. One cause of this phenomenon is that the clearance Froude number is deemed to be in the transcritical regime when it is in proximity to 1.0 [25]. The resonance effect comes into play especially at a low altitude. The other one is the wave-making effect caused by the deformation of the free surface; the wave-making effect is significant at a low clearance Froude number interval. When the clearance Froude number is less than 0.4 (the clearance is larger than the length of the generated free surface wave), the wave-making effect can be neglected [31]. When the clearance Froude number is greater than 5.0, the length of the generated free surface wave is much greater than the chord length. Accordingly, the ratio of C_L to C_{LR} is approximately independent of the clearance Froude number, and the ratio tends to be equal to 1; then the wave-making effect is insignificant. This result is in good agreement with the conclusion obtained by Barber [16], who states that the Froude number is large enough to prevent any wave deformation from occurring. Consequently, the reason for the sharp variation in the lift coefficient at $\mathrm{Fr}_h = 1.0$ is the coupling of the resonance effect and the essential wave-making effect at a low Froude number interval.

In reality, the chord length is on the order of meters, say, 1 m. Then the condition $\mathrm{Fr}_h = 1$ requires the velocity of the wing to equal approximately 3 m/s. This speed is far less than normal cruising velocity of between 100 and 200 m/s, and the corresponding Froude number is greater than 35. Thus, this condition $\mathrm{Fr}_h = 1$ only occurs at the takeoff or landing stage, and it can be argued that the free surface can safely be treated as rigid at the cruising stage.

Consider the lift coefficient for a wing with a dihedral operating above a free surface in subsonic flow varying with the dihedral angle as shown in Fig. 7. It is assumed that the attack angle is equal to 5°, and the aspect ratio equals 4.0. Figure 7 clearly shows the lift coefficient as a function of the dihedral angle for different values of clearance-to-chord ratio h/c and Mach numbers of 0.4 and 0.6. The abscissa represents the value of the dihedral angle, and the ordinate denotes the lift coefficient. It can be observed from Fig. 7 that when the wing is out of ground effect, the lift coefficient is a decreasing function of the absolute value of the dihedral angle. However, when

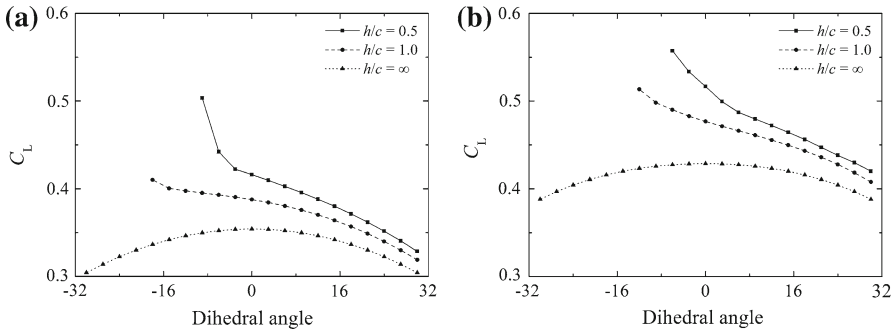

Fig. 7 Performance of lift coefficient versus dihedral angle at different h/c for Mach numbers of **a** $M_a = 0.4$ and **b** $M_a = 0.6$

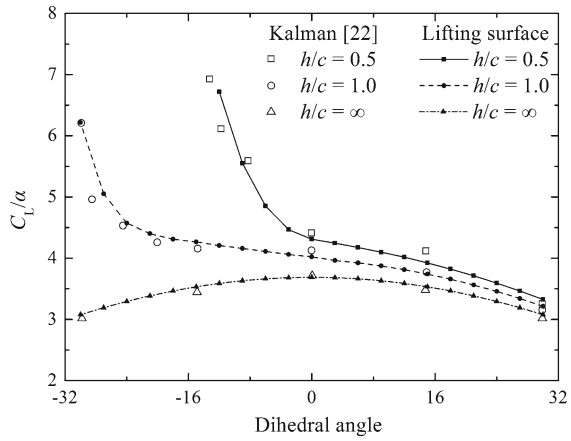

Fig. 8 Comparison between present (*line and symbol*) and Kalman et al. [22] (*hollow dot*) solution for lift coefficient divided by α as a function of dihedral angle at an aspect ratio of 4.0

the wing is in the vicinity of a free surface, the lift coefficient increases dramatically with diminishing altitude, especially in cases where the dihedral angle is less than zero. This is because the tips of the wing are much closer to the free surface while the dihedral angle is less than zero. In other words, WIG effect is more significant in that case. Therefore, a WIG effect craft can benefit immensely if the coupling of the dihedral effect and WIG effect are fully utilized. We also find from Fig. 7 that the compressibility of air has a significant influence on the lift coefficient, registered as increasing with Mach number, especially at a low altitude.

Figure 8 presents a comparison of the lift curve slope (lift coefficient divided by attack angle) for a dihedral wing with an aspect ratio of 4.0 and an angle of attack of 5.0° in proximity to a rigid wall between the present method and the doublet-lattice method carried out by Kalman et al. [22]. In this step, in validating the numerical results, the compressibility of the air is neglected. Figure 8 shows the lift curve slope as a function of the dihedral angle at different clearance-to-chord ratios h/c. The abscissa is the dihedral angle, and the ordinate denotes the lift coefficient. The line and symbol in Fig. 8 represent the present work, and the hollow dot denotes the results calculated using the doublet-lattice method in Ref. [22]. Agreement with the results given by Kalman et al. [22] is rather good.

Figure 9 presents the lift performance for a swept wing whose aspect ratio is 4.0 and attack angle equals 5.0°, traveling in proximity to a free surface varying with sweep angle at different clearance-to-chord ratios h/c for Mach numbers of 0.4 and 0.6. In Fig. 9, the abscissa denotes the sweep angle, and the ordinate represents the lift coefficient.

We find from Fig. 9 that the lift coefficient for an unswept wing is always larger than that of a swept wing regardless of whether the wing is located in or out of ground effect. Thus, it seems that a wing with a swept geometry is unnecessary for WIG effect craft if the compressibility effect is ignored. However, it can be concluded that a high Mach number has a more significant influence on the lift performance registered as an increase in the lift coefficient by contrasting (Fig. 9a and b).

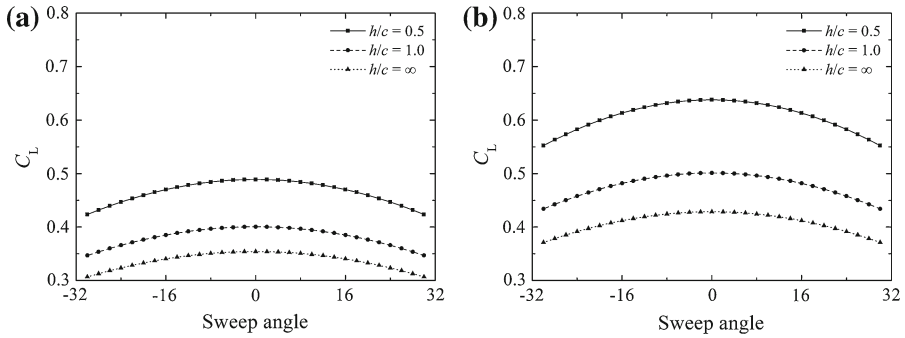

Fig. 9 Properties of lift coefficient versus sweep angle at different h/c for Mach numbers of **a** $M_a = 0.4$ and **b** $M_a = 0.6$

8 Conclusions

We have presented a computational procedure for determining the lift properties of curved wings operating in the vicinity of a free surface. We started from fully nonlinear governing equations, separately for air and water. For the free surface boundary conditions, the fully nonlinear kinematic and dynamic conditions were deduced. The perturbation technique was used to linearize the governing equations and the free surface boundary conditions. An established technique is to find the Green's function for the three-dimensional horseshoe vortex operating above a free surface in a stratified fluid, where the air is regarded as being weakly compressible, but the water is incompressible.

For lift performance, as expected, the compressibility played a significant role, registered as the lift increasing with the Mach number in the subsonic regime. Unlike the dihedral wing out-of-ground effect, the lift can reach a very high value as the dihedral angle is less than zero while the wing is subject to the WIG effect craft. Thus, WIG effect craft can benefit significantly if the dihedral effect is fully utilized. The lift for an unswept wing is always larger than that of a swept wing regardless of whether or not the wing is subject to a WIG effect. Therefore, the swept effect is unprofitable from the lift performance point of view. Furthermore, the following conclusions can be drawn:

(a) The free surface elevation is rather small and can safely be regarded as a rigid wall due to the small air–water density ratio if the clearance between the wing and the free surface has the same order as the length.
(b) The lift fluctuates sharply with the Froude number at a low altitude, which is mainly caused by the wave-making effect and the resonance while the clearance Froude number is low. In other words, the free surface disturbance effect is significant for takeoff and landing. At the cruising stage, the free surface can be safely treated as a rigid wall.

Acknowledgments The authors acknowledge the anonymous reviewers for their critical comments and suggestions that improved the manuscript considerably. The present work is supported by the National Natural Science Foundation of China (50921001, 51279030, and 50909017), National Key Basic Research Special Foundation of China (2010CB832704 and 2013CB036101), and Scientific Project for High-Tech Ships: Key Technology Research on Semi-planning Fore-placed-outrigger Trimaran.

Appendix 1

In this part, we aim to verify that the elevation of a free surface is small. Based on the one-dimensional continuity equation, we have [32]

$$Uh = \left(U + \frac{\partial \varphi_a}{\partial x}\right)[h - t(x, y) - \zeta(x, y)]. \tag{72}$$

Thus, the free surface elevation can be obtained from Eq.(72):

$$\zeta\left(x,y\right)=h-t\left(x,y\right)-\frac{Uh}{U+\frac{\partial\varphi_a}{\partial x}}. \tag{73}$$

Based on Bernoulli equation in (7), the free surface elevation can be expressed in the form

$$\begin{aligned}\zeta\left(x,y\right)=&-\frac{\rho_w}{g\left(\rho_w-\rho_a\right)}\left[U\frac{\partial\varphi_w}{\partial x}+\frac{1}{2}\left(\frac{\partial\varphi_w}{\partial x}\right)^2+\frac{1}{2}\left(\frac{\partial\varphi_w}{\partial y}\right)^2+\frac{1}{2}\left(\frac{\partial\varphi_w}{\partial z}\right)^2\right]\\&+\frac{\rho_a}{g\left(\rho_w-\rho_a\right)}\left[U\frac{\partial\varphi_a}{\partial x}+\frac{1}{2}\left(\frac{\partial\varphi_a}{\partial x}\right)^2+\frac{1}{2}\left(\frac{\partial\varphi_a}{\partial y}\right)^2+\frac{1}{2}\left(\frac{\partial\varphi_a}{\partial z}\right)^2\right].\end{aligned} \tag{74}$$

Due to the small density ratio of air to water, the density ratio can be expressed as

$$\frac{\rho_a}{\rho_w}=\delta_1\rho, \tag{75}$$

where ρ is an $O(1)$ quantity. By substituting asymptotic expansions of the velocity potentials in air and water in Eqs. (17) and (18) into Eq. (74) and preserving the first-order expression, we can obtain

$$\zeta(x)=-\frac{\delta_1 U\frac{\partial\varphi_w^{(1)}}{\partial x}}{g\left(1-\delta_1\rho\right)}. \tag{76}$$

From Eq. (76), it can be argued that the free surface deformation induced by the foil has the same order as δ_1.

Appendix 2

In this part, we aim to derive the perturbed velocity components induced by the vortex filament with an arbitrary contour in the subsonic regime using the Biot–Savart law, which reads

$$\mathbf{u}=-\frac{\Gamma}{4\pi}\int_C\frac{\mathbf{R}\times\mathrm{d}\mathbf{l}}{R^3}. \tag{77}$$

Due to the scale stretching of the x coordinate in the subsonic flow, the vectors $\mathbf{R}$ and $\mathrm{d}\mathbf{l}$ can be expressed as

$$\mathbf{R}=\left(\frac{x-\xi}{\beta},\ y-\eta,\ z-\zeta\right) \tag{78}$$

and

$$\mathrm{d}\mathbf{l}=\left(\frac{1}{\beta}\mathrm{d}\xi,\ \mathrm{d}\eta,\ \mathrm{d}\zeta\right). \tag{79}$$

Thus, the perturbed velocity components in the Ox, Oy, and Oz directions are

$$u=-\frac{\Gamma}{4\pi}\int_C\frac{\left(y-\eta\right)\mathrm{d}\zeta-\left(z-\zeta\right)\mathrm{d}\eta}{\left[\left(\frac{x-\xi}{\beta}\right)^2+\left(y-\eta\right)^2+\left(z-\zeta\right)^2\right]^{3/2}}=\frac{\Gamma}{4\pi}\int_C\frac{\partial}{\partial y}\left(\frac{1}{R}\right)\mathrm{d}\zeta-\frac{\partial}{\partial z}\left(\frac{1}{R}\right)\mathrm{d}\eta, \tag{80}$$

$$v=-\frac{\Gamma}{4\pi}\int_C\frac{\left(z-\zeta\right)\frac{\mathrm{d}\xi}{\beta}-\left(\frac{x-\xi}{\beta}\right)\mathrm{d}\zeta}{\left[\left(\frac{x-\xi}{\beta}\right)^2+\left(y-\eta\right)^2+\left(z-\zeta\right)^2\right]^{3/2}}=\frac{\Gamma}{4\pi}\int_C\frac{1}{\beta}\frac{\partial}{\partial z}\left(\frac{1}{R}\right)\mathrm{d}\xi-\beta\frac{\partial}{\partial x}\left(\frac{1}{R}\right)\mathrm{d}\zeta, \tag{81}$$

and

$$w = -\frac{\Gamma}{4\pi}\int_C \frac{\left(\frac{x-\xi}{\beta}\right)\mathrm{d}\eta - (y-\eta)\,\frac{\mathrm{d}\xi}{\beta}}{\left[\left(\frac{x-\xi}{\beta}\right)^2 + (y-\eta)^2 + (z-\zeta)^2\right]^{3/2}} = \frac{\Gamma}{4\pi}\int_C \beta\frac{\partial}{\partial x}\left(\frac{1}{R}\right)\mathrm{d}\eta - \frac{1}{\beta}\frac{\partial}{\partial y}\left(\frac{1}{R}\right)\mathrm{d}\xi. \tag{82}$$

References

1. Han C, Cho J (2005) Unsteady trailing vortex evolution behind a wing in ground effect. J Aircr AIAA 42:429–434
2. Raymond AE (1921) Ground influence on airfoils. NACA Technical Note 67
3. Pozrikidis C (2009) Fluid dynamics: theory, computation, and numerical simulation, 2nd edn. Springer, New York
4. Ahmed MR, Sharma SD (2005) An investigation on the aerodynamics of a symmetrical airfoil in ground effect. Exp Therm Fluid Sci 29:633–647
5. Zhang X, Zerihan J (2003) Off-surface aerodynamic measurements of a wing in ground effect. J Aircr AIAA 40:716–725
6. Ahmed MR, Takasaki T, Kohama Y (2007) Aerodynamics of a NACA 4412 airfoil in ground effect. AIAA J 45:37–47
7. Iosilevskii G (2008) Asymptotic theory of an oscillating wing section in weak ground effect. Eur J Mech B–Fluid 27:477–490
8. Widnall SE, Barrows TM (1970) An analytic solution for two- and three-dimensional wing in ground effect. J Fluid Mech 41:769–792
9. Han C, Kim H, Cho J (2006) Steady aerodynamic characteristics of a wing flying over a nonplanar ground surface Part I: rail. J Mar Sci Tech 20:1043–1050
10. Han C, Kim H, Cho J (2006) Steady aerodynamic characteristics of a wing flying over a nonplanar ground surface Part II: channel. J Mar Sci Tech 20:1051–1058
11. Dragos L (1990) Subsonic flow past thick wing in ground effect, lifting line theory. Acta Mech 82:49–60
12. Park K, Lee J (2008) Influence of endplate on aerodynamic characteristics of low-aspect-ratio wing in ground effect. J Mech Sci Tech 22:2578–2589
13. Moryossef Y, Levy Y (2004) Effect of oscillations on airfoils in close proximity to ground. AIAA J 42:1755–1754
14. Rozhdestvensky K (2006) WIG vehicles. Prog Aerosp Sci 42:211–283
15. Suzuki K, Ikehata M (1994) Free surface effect of wig advancing over the still water surface. Proceedings of the International Conference on Hydrodynamics (ICHD'94), pp 254–260
16. Barber TJ (2007) A study of water surface deformation due to tip vortices of a WIG. J Ship Res 51:182–186
17. Zong Z, Liang H, Zhou L (2012) Lifting line theory for wing-in-ground effect in proximity to a free surface. J Eng Math 74:143–158
18. Liang H, Zhou L, Zong Z, Sun L (2013) An analytical investigation of two-dimensional and three-dimensional biplanes operating in the vicinity of a free surface. To appear in J Mar Sci Tech. doi:0.1007/s00773-012-0187-9
19. Katz J, Plotkin A (1991) Low-speed aerodynamics: from wing theory to panel method. McGraw-Hill, Singapore
20. Sachs G, Holzapfel F (2007) Flight mechanic and aerodynamic aspects of extremely large dihedral in birds. AIAA J 46:1–12
21. Phillips WF, Hansen AB, Nelson WM (2006) Effects of tail dihedral on static stability. J Aircr AIAA 43:1829–1837
22. Kalman TP, Rodden WP, Giesing J (1971) Application of the doublet-lattice method to nonplanar configurations in subsonic flow. J Aircr AIAA 8:406–413
23. Gulcat U (2010) Fundamentals of modern unsteady aerodynamics. Springer, Berlin
24. Milne-Thomson LM (1973) Theoretical aerodynamics. Dover, New York
25. Newman JN (1977) Marine hydrodynamics. MIT, Cambridge
26. Scullen DC, Tuck EO (2011) Free-surface elevation due to moving pressure distributions in three dimensions. J Eng Math 70:29–42
27. Yeung RW, Nguyen TC (1999) Waves generated by a moving source in a two-layer ocean of finite depth. J Eng Math 35:85–107
28. Abramowitz M, Stegun IA (1972) Handbook of mathematical functions. Dover, New York
29. Noblesse F (1981) Alternative integral representations for the Green function of the theory of ship wave resistance. J Eng Math 15:241–265
30. Smith AMO, Giesing JP, Hess JL (1963) Calculation of waves and wave resistance for bodies moving on or beneath the surface of the sea. Douglas Aircraft Co., Long Beach, Report No 31488a
31. Faltinsen OM (2005) Hydrodynamics of high-speed marine vehicles. Cambridge University Press, Cambridge
32. Tuck EO (1984) A simple one-dimensional theory for air-supported vehicles over water. J Ship Res 28:290–292